nature communications

Article

https://doi.org/10.1038/s41467-025-58163-0

Atomic-scale self-rearrangement of hetero-metastable phases into high-density single-atom catalysts for the oxygen evolution reaction

Received: 13 June 2024

Accepted: 13 March 2025

Published online: 25 March 2025

Check for updates

Quan Quan[1,10], Yuxuan Zhang[1,10], Haifan Li[2], Wei Wang[1], Pengshan Xie[1], Dong Chen[1], Weijun Wang[1], You Meng[1,3], Di Yin[1], Yezhan Li[1], Dongyuan Song[4], Lijie Chen[5], Shaohai Li[6,9] ✉, Cheng Yang[6], Takeshi Yanagida[7,8], Chun-Yuen Wong[2], SenPo Yip[7] ✉ & Johnny C. Ho[1,3,7] ✉

Maximizing metal-substrate interactions by self-reconstruction of coadjutant metastable phases can be a delicate strategy to obtain robust and efficient high-density single-atom catalysts. Here, we prepare high-density iridium atoms embedded ultrathin CoCeOOH nanosheets (CoCe-O-Ir_{SA}) by the electrochemistry-initiated synchronous evolution between metastable iridium intermediates and symmetry-breaking $CoCe(OH)_2$ substrates. The CoCe-O-Ir_{SA} delivers an overpotential of 187 mV at 100 mA cm^{-2} and a steady lifespan of 1000 h at 500 mA cm^{-2} for oxygen evolution reaction. Furthermore, the CoCe-O-Ir_{SA} is applied as a robust anode in an anion-exchange-membrane water electrolysis cell for seawater splitting at 500 mA cm^{-2} for 150 h. Operando experimental and theoretical calculation results demonstrate that the reconstructed thermodynamically stable iridium single atoms act as highly active sites by regulating charge redistribution with strongly *p-d-f* orbital couplings, enabling electron transfer facilitated, the adsorption energies of intermediates optimized, and the surface reactivity of Co/Ce sites activated, leading to high oxygen evolution performance. These results open up an approach for engineering metastable phases to realize stable single-atom systems under ambient conditions toward efficient energy-conversion applications.

Developing high-performance oxygen evolution reaction (OER) electrocatalysts is core to the renewable energy-related conversion processes (e.g., water electrolysis, metal-air batteries, carbon dioxide reduction, and nitrogen reduction), which generally require a large overpotential to overcome its sluggish kinetics[1]. Single-atom catalysts (SACs) feature spatially isolated metal atoms and maximized atomic utilization efficiency, sparking enormous interest as a class of promising materials[2]. In this regard, high-density SACs have been pursued to increase the number of available active sites to maximize OER performance[3]. However, the individual metal atoms generally tend to agglomerate into clusters or nanoparticles through the Ostwald ripening process owing to the weak metal-substrate interactions, especially for densely populated single atoms (SAs)[4]. Besides, the SAs are prone to segregation from the support due to weak interactions with substrates during the OER, resulting in decreased stability[5]. Therefore, it is urgent to simultaneously address the challenges of

A full list of affiliations appears at the end of the paper. ✉e-mail: sh09.li@nus.edu.sg; yip.sen.po.472@m.kyushu-u.ac.jp; johnnyho@cityu.edu.hk

high-density loadings and instability of SACs towards achieving high OER activity and durability.

The preparation of SACs reversely using nanoparticle or cluster-scale precursors is rarely reported because of the increased thermodynamic entropy, requiring harsh reaction conditions and strong substrate interactions. For instance, Pt clusters can be converted into SAs encapsulated by a high-silica chabazite substrate based on an atmosphere-induced metal dispersion mechanism[6]. Under a confinement anchor effect, stable Ag SAs were fabricated from the fragmentation of Ag particles using a facet-reconstructed MnO_2 substrate assisted by thermal treatment[7]. The limited intimate physical interface between the precursors and substrates makes realizing the high-density SAs loading challenging[8]. Local or long-range structural reconstructions generally occur on transition metal-based catalysts during the electrocatalytic OER processes at mild conditions, accompanied by the atomic arrangements[9]. Therefore, the structural evolution potentially involves numerous anchoring sites that endow the fragment of adsorbed metastable species into the encased SAs with a low formation energy[10]. Currently, little attention has been paid to utilizing the interactive self-reconstruction between mixed metastable phases to produce thermodynamically stable high-density SAs incorporated systems for high-performance OER applications.

In this work, as a proof of concept, taking an "atomic-scale self-rearrangement" strategy with an anti-Ostwald ripening process under ambient conditions, we prepared high-density Ir SAs confined into the ultrathin CoCeOOH nanosheets (CoCe–O–Ir_{SA}) evolved from the metastable Ir species on the symmetry-breaking $CoCe(OH)_2$ substrates during the OER as a model, confirmed by aberration-corrected scanning transmission electron microscopy and X-ray absorption spectroscopy. In-situ characterization and theoretical calculation results demonstrate that the embedded Ir SAs act as highly active centers for facilitating electron transfer by strongly *p*–*d*–*f* orbital couplings, optimizing the adsorption energies for catalytic intermediates, and activating the surface reactivity of Co/Ce sites. Notably, the CoCe–O–Ir_{SA} exhibits a high OER performance with an overpotential of 187 mV at 100 mA cm^{-2} and steady operation for 1000 h at 500 mA cm^{-2}, which is superior to state-of-the-art reported electrocatalysts at this current-density level. Moreover, the CoCe–O–Ir_{SA} growth on nickel foam is directly applied in an anion-exchange-membrane water electrolysis (AEMWE) system as an anode for seawater splitting, and steady operation is realized at a high-current density of 500 mA cm^{-2} for 150 h. Our work has provided an innovative and simple method to stabilize the densely populated monatomic iridium with high stability and activity.

Results and discussion

The CoCe–O–Ir heterostructure model is synthesized by a facile two-step strategy at room temperature. First, the cobalt-cerium hydroxides (denoted as CoCe) nanosheet arrays substrate is in situ grown on the nickel foam (NF) in a moderate alkaline environment (Supplementary Fig. 1). Then, the Ir-based metastable intermediates, including clusters and SAs are uniformly co-formed on the surface of CoCe nanosheet arrays (denoted as CoCe–O–Ir) by the facile wet-chemistry impregnation method followed by a low-temperature drying treatment. The negatively charged surface sites of CoCe can spontaneously drive the electrostatic adsorption of ($IrCl_x^+$) complex cations. Moreover, the slow hydrolysis of the complex during the mild synthesis process further induces the co-growth of IrO_x clusters and Ir SAs[11]. In Fig. 1a, the scanning electron microscopy (SEM) image shows that the interconnected CoCe–O–Ir nanosheets are vertically aligned on the surface of the NF skeleton, well-preserved from the sheet-array structure of the CoCe precursors (Supplementary Fig. 2), providing abundant open channels and fully exposed active sites for surface-mediated electrocatalytic reactions[12].

The transmission electron microscopy (TEM) image discloses that the numerous well-dispersed clusters with a dark contrast have an average size of 1.75 nm (Fig. 1b and Supplementary Fig. 3). Moreover, the atomic force microscopy (AFM) image and corresponding height statistics reveal an ultrathin feature of CoCe–O–Ir nanosheets with an average thickness of 4.4 nm (Supplementary Fig. 4). The high-angle annular dark-field scanning transmission electron microscopy (HAADF-STEM) image and corresponding elemental mapping demonstrate the homogenous distribution of Co, Ce, and Ir elements throughout the nanosheet (Fig. 1c). The atomic-scale structures were further explored by aberration-corrected HAADF-STEM (AC-HAADF-STEM). As shown in Fig. 1d, a few nanosized clusters (highlighted by the yellow dashed circles) and abundant isolated bright spots were detected. In detail, for region i, the lattice fringes of the cluster possess a d-spacing of 2.6 Å, attributed to the (011) plane of IrO_2 (Fig. 1e)[13]. Meanwhile, for region ii, the isolated bright spots confirm the existence of atomically dispersed Ir on the surface of the $CoCe(OH)_2$ substrate (Fig. 1f). Therefore, these results indicate the well-dispersed IrO_x clusters and Ir SAs are co-formed on the CoCe nanosheets.

The X-ray diffraction (XRD) patterns of Co and CoCe samples display the typical diffraction peaks corresponding to the (003) and (006) planes of layered hydroxides, indicating the successful synthesis of single-phase layered hydroxides intercalated with NO_3^- anions (Supplementary Fig. 5)[14]. After the co-introduction of IrO_x clusters and Ir SAs, the XRD pattern of CoCe–O–Ir exhibits a single broad (006) peak with decreased intensity, which can be ascribed to the fact that the hydrolysis process of adsorbed $IrCl_x$ breeds new coordination bonds between the Ir intermediates and CoCe substrates with the self-provided alkaline environment, resulting in the symmetry breaking of CoCe substrates. Besides, there are no peaks corresponding to IrO_2 and metallic Ir, suggesting the ultrafine size of IrO_x and good dispersion of Ir SAs, respectively[15].

The chemical composition and valence states at the surface of CoCe and CoCe–O–Ir were further investigated by X-ray photoelectron spectroscopy (XPS). The high-resolution Co 2*p* spectra in Fig. 1g reveal two valent states of Co^{3+} and Co^{2+} in CoCe and CoCe–O–Ir. Specifically, the CoCe sample shows the peaks for Co^{3+} (780.97 and 796.65 eV) and Co^{2+} (783.29 and 798.39 eV)[16], while it delivers negative shifts after the introduction of IrO_x clusters and Ir SAs. Meanwhile, the high-resolution Ce 3*d* spectra exhibit multiplet splitting of Ce^{3+} and Ce^{4+}, demonstrating the existence of two valent states for the cerium species in CoCe and CoCe–O–Ir (Supplementary Fig. 6)[17]. Similarly, the binding energies in Ce 3*d* region of CoCe also shift after the hybridization. The charge redistribution indicates the existence of strong electronic interactions between the CoCe supports with IrO_x clusters and Ir SAs. For the Ir 4*f* spectrum of CoCe–O–Ir, the peaks locate at 62.06 and 64.98 eV, suggesting that the oxidation state accounts for the majority of Ir species (Fig. 1h)[18].

To gain deeper insight into the electronic states and coordination environment of Ir atoms, X-ray absorption fine structure (XAFS) measurements were performed. As shown in Ir L_3-edge X-ray absorption near edge structure (XANES) spectra (Fig. 1i), the white-line intensity increases in the order: Ir foil < CoCe–O–Ir < IrO_2, further demonstrating an oxidation electronic structure of Ir in the Co–Ce–O–Ir sample[19]. Then, the valence state of Ir is quantitatively calculated by the integration of the white-line peak in differential XANES spectra (ΔXANES), which is obtained by subtracting the spectrum from that of the Ir foil[20]. The average valence state of Ir is +3.37 in the CoCe–O–Ir sample (Fig. 1j and Supplementary Fig. 7). Furthermore, the atomic coordination configuration of Ir is determined by Fourier transform extended X-ray absorption fine structure spectroscopy (FT-EXAFS) (Fig. 1k) and corresponding fitting results (Supplementary Fig. 8 and Supplementary Table 1). There are two peaks at 2.01 and 2.34 Å for CoCe–O–Ir, which can be ascribed to Ir–O and Ir–Cl bonds, respectively. The Ir–Cl bond comes from the deposited $IrCl_x$ species[21]. The Ir–O bond is

https://doi.org/10.1038/s41467-025-58163-0

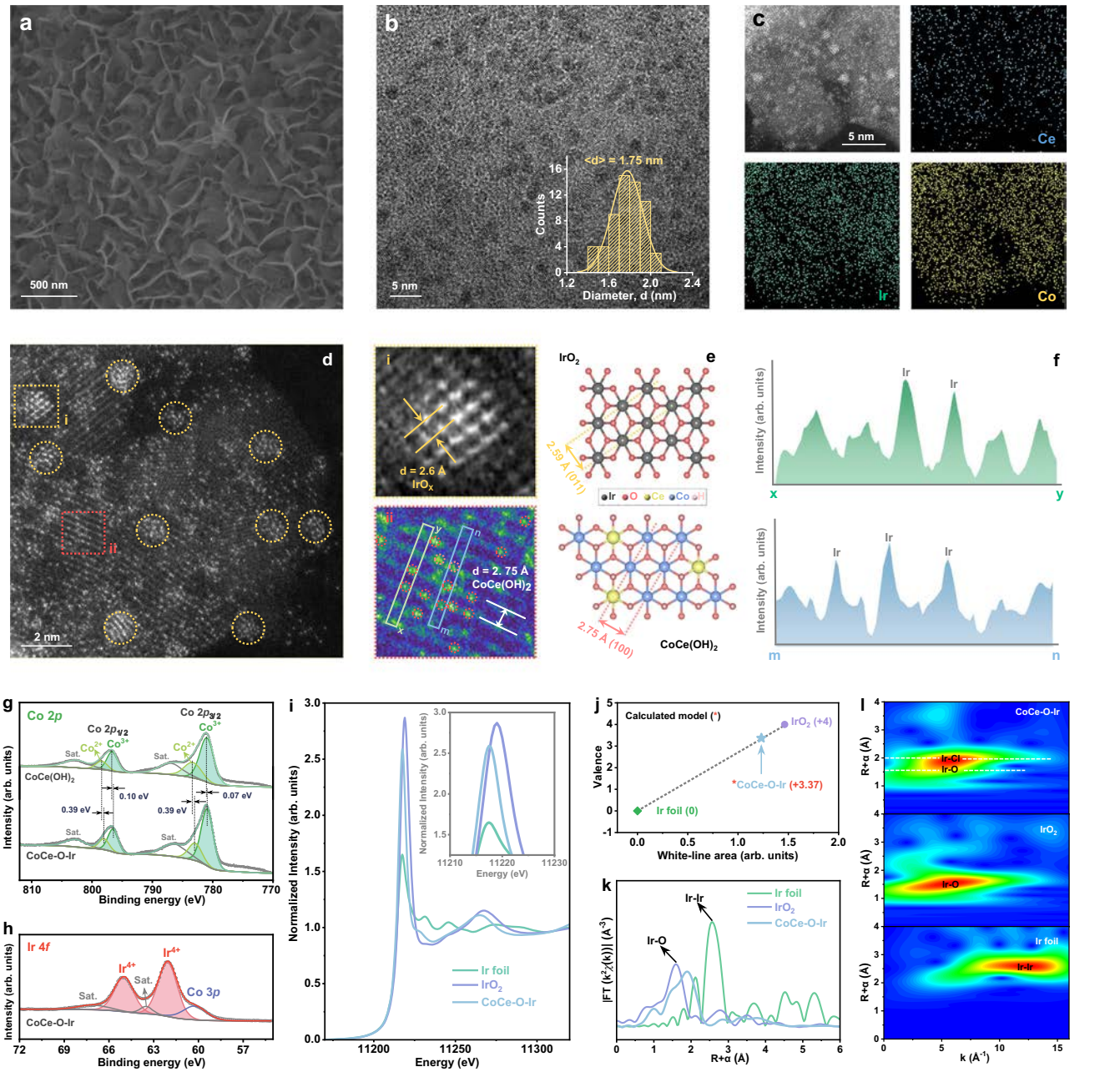

Fig. 1 | Material characterizations of CoCe–O–Ir nanosheet arrays. a SEM image. **b** TEM image and corresponding statistical calculation for cluster diameter. **c** HAADF-STEM image and corresponding elemental mapping. **d** AC-HAADF-STEM image. The spots in the yellow dashed circles are ascribed to the IrO_x clusters. **e** Enlarged AC-HAADF-STEM image from regions i and ii in (**d**) highlighted with yellow and red dashed boxes and standard structural models. The spots in the red dashed circles are ascribed to Ir SAs. **f** The extracted line profiles from region ii in (**e**) highlighted with green (x-y) and blue (m-n) rectangles. **g** Co 2*p* XPS spectra of CoCe and CoCe–O–Ir. **h** Ir 4*f* XPS spectrum of CoCe–O–Ir. The sat. in (**g**, **h**) is the abbreviation of satellite peak. **i** Normalized XANES at the Ir L_3-edge of Ir foil, IrO_2, and CoCe–O–Ir. **j** Calculated Ir oxidation states. The arb. units in (**f**–**j**) is the abbreviation of arbitrary units. **k** Corresponding FT-EXAFS curves. **l** EXAFS wavelet transform plots. The R + α in (**k**, **l**) is the radical distance; the **κ** in (**k**, **l**) is the wave vector. Source Data are provided as a Source Data file.

generated by coordinating the co-formed IrO_x clusters and Ir SAs with the CoCe substrates. Meanwhile, the Ir–M bond (M = Ir, Co, or Ce) is not detected, eliminating the existence of Ir metallic clusters[22]. The Ir atoms are not directly coordinated with metal sites in CoCe, which is further confirmed by the Wavelet transform plots (Fig. 1l)[23].

Afterward, the electrochemical OER performance of CoCe–O–Ir was evaluated by a typical three-electrode setup in an Ar-saturated alkaline solution (1.0 M KOH) (Supplementary Fig. 9). By tuning the Ir loading amounts, the optimal CoCe–O–Ir sample for OER performance was applied in subsequent tests, and the detailed results are displayed in Supplementary Figs. 10–12. For comparison, the Co–O–Ir, CoCe, Co, and pure NF as counterparts and commercial IrO_2 as a benchmark were tested under identical conditions. The corresponding polarization curves without *iR* correction were provided in Supplementary Fig. 13 as a reference. As depicted in Fig. 2a, the CoCe–O–Ir heterostructure exhibits the highest OER activity compared to the other samples. Specifically, the CoCe–O–Ir only requires an overpotential of 187 mV to deliver a current density of 100 mA cm^{-2}, while the required overpotentials are 238 mV for Co–O–Ir, 285 mV for CoCe, 313 mV for Co, 381 mV for IrO_2, and 521 mV for NF to reach 100 mA cm^{-2}. More impressively, the CoCe–O–Ir delivers high-current densities of 500 mA cm^{-2} at an overpotential of 217 mV, which is also superior to

https://doi.org/10.1038/s41467-025-58163-0

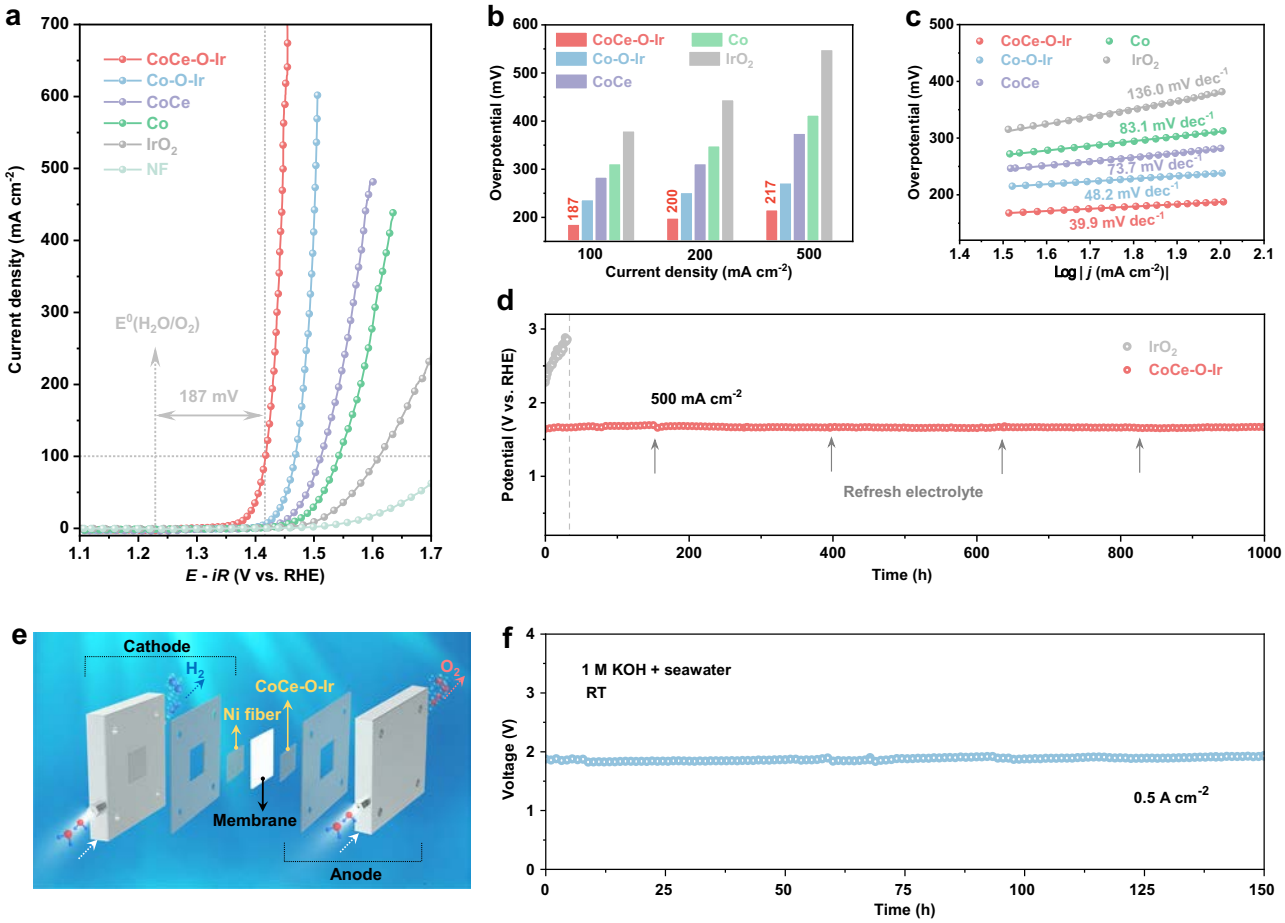

Fig. 2 | Evaluation of electrocatalytic OER performance. a Polarization curves with *iR* correction in 1.0 M KOH. **b** Overpotentials comparison at different current densities. **c** Tafel plots. **d** CP curves of CoCe–O–Ir and IrO_2 without *iR* correction at 500 mA cm^{-2}. **e** Schematic of the AEMWE configuration. **f** Durability cell voltage-time curve for seawater splitting without *iR* correction. The RT in (**f**) represents room temperature. Source Data are provided as a Source Data file.

those of the referenced samples (Fig. 2b). The inconspicuous OER performance of commercial IrO_2 could be ascribed to its large particle size and aggregation on the substrate (Supplementary Fig. 14). In turn, it is pinpointed that the aligned nanosheet-array structure can increase the exposure of active sites and mass transfer to boost the surface-mediated electrocatalytic reactions.

Additionally, the values of Tafel slopes are calculated to be 39.9, 48.2, 73.7, 83.1, and 136.0 mV dec^{-1} for CoCe–O–Ir, Co–O–Ir, CoCe, Co, and IrO_2, respectively (Fig. 2c). The CoCe–O–Ir with the lowest Tafel slope exhibits the most rapid OER kinetics. Moreover, the Nyquist plots reveal that the CoCe–O–Ir features the smallest charge-transfer resistance compared to the three counterparts (Supplementary Fig. 15). Besides, the electrochemical surface areas (ECSA) of various samples are further estimated from the electrochemical double-layer capacitance (C_{dl}). The largest C_{dl} value of CoCe–O–Ir among all catalysts illustrates the maximum density of catalytically active sites, promoting the intrinsic OER activity (Supplementary Figs. 16 and 17).

In the following, chronopotentiometry (CP) tests were conducted under a high-current density of 500 mA cm^{-2} to assess the stability of CoCe–O–Ir nanosheet arrays and commercial IrO_2. The potential of CoCe–O–Ir remains essentially stable throughout the constant operation for 1000 h, while the potential of commercial IrO_2 increases quickly after only 30 h (Fig. 2d). Meanwhile, the morphology of nanosheet arrays is well-maintained after the stability test (Supplementary Figs. 18 and 19), demonstrating the superior OER durability of CoCe–O–Ir nanosheet arrays in the alkaline media. In this way, the CoCe–O–Ir catalyst delivers a high OER performance as compared with other state-of-the-art electrocatalysts from recent literature, covering several kinds of systems (i.e., LDH-based materials, noble metal-involved materials, and noble metal-hydroxides composites) (Supplementary Tables 2–4). To demonstrate the practicability for a harsher condition, the overall seawater splitting is conducted using an anion-exchange-membrane water electrolysis (AEMWE) cell with the CoCe–O–Ir nanosheet arrays on NF as anode coupling with a commercial cathode (NiFeCo/Ni fiber) (Fig. 2e). The AEMWE system delivers a cell voltage of 1.92 V to reach a current density of 0.5 A cm^{-2}, which is about three times higher than the reached current density of a cell using IrO_2/NF||NiFeCo/Ni fiber couple at an identical cell voltage (Supplementary Fig. 20). The faradaic efficiency of CoCe–O–Ir_{SA} for O_2 generation is determined to be 99.3 % for seawater splitting, suggesting a high selectivity toward OER activity (Supplementary Fig. 21). The as-constructed AEMWE electrolyzer can sustain stable performance under 0.5 A cm^{-2} for 150 h in alkaline seawater (Fig. 2f), further confirming the good durability of the CoCe–O–Ir nanosheet arrays and its viability for real seawater electrolysis[24].

To explore the active structure for boosting the OER, potential-dependent in-situ Raman spectroscopy on CoCe–O–Ir was implemented with a magnitude of 50 mV (Fig. 3a). As the applied potential increases from 1.00 to 1.50 V vs. RHE, the Raman peaks at around 470 and 580 cm^{-1} were detected with the intensities gradually enhanced, which is also clearly presented by the corresponding contour plots (Fig. 3b). These two peaks are correlated to the E_g bending and A_{1g} stretching vibrations of the M–O (M = Co, Ce, or Ir) bond in MOOH species[25,26], demonstrating that the in-situ formed oxyhydroxide

https://doi.org/10.1038/s41467-025-58163-0

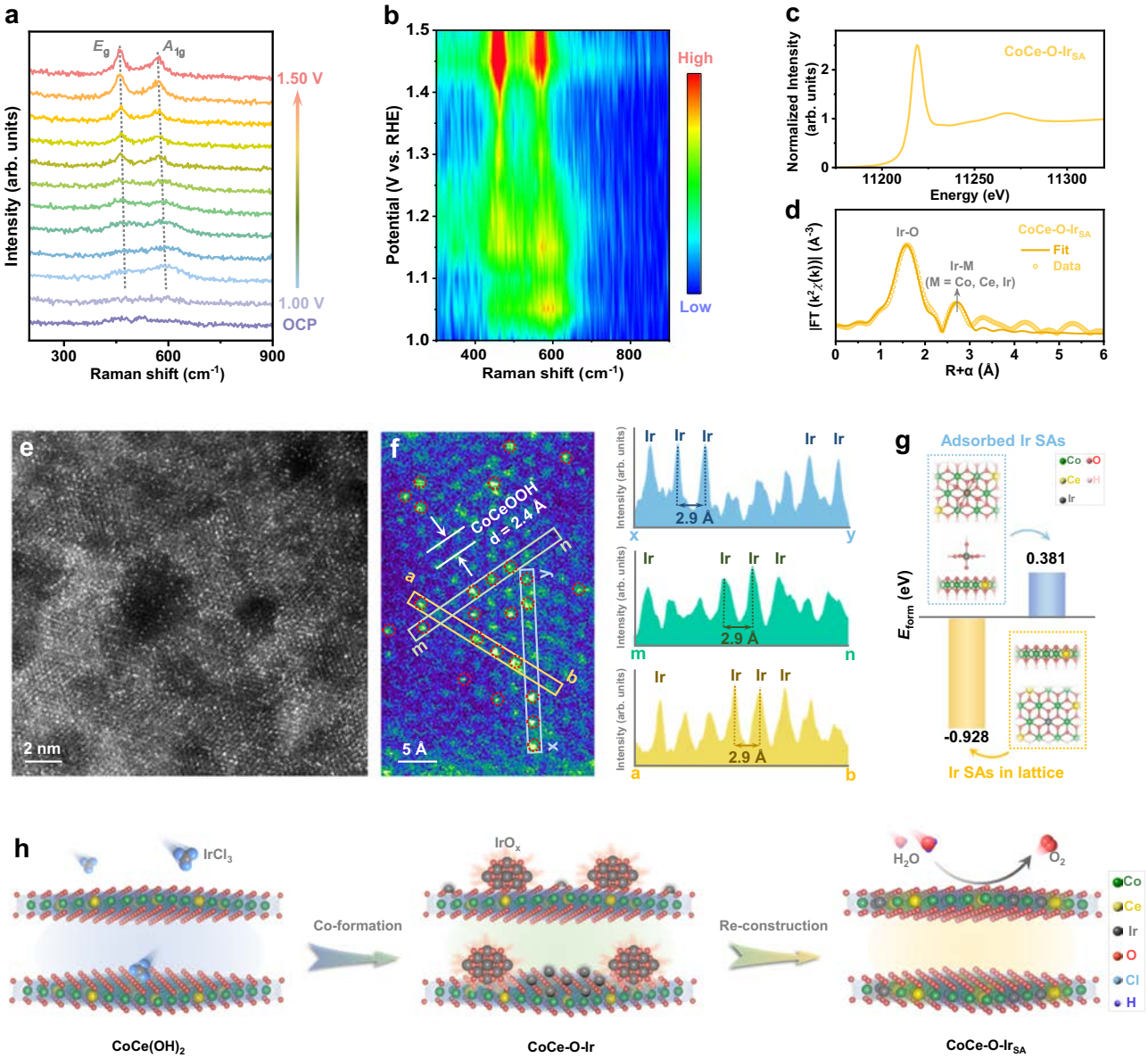

Fig. 3 | Identification of the active structures. Potential-dependent in-situ Raman spectra (**a**) and corresponding contour plots (**b**). **c** The normalized XANES at the Ir L_3-edge of CoCe–O–Ir_{SA}. **d** FT-EXAFS fitting curve of CoCe–O–Ir_{SA}. **e** AC-HAADF-STEM image of CoCe–O–Ir_{SA}. **f** A magnified AC-HAADF-STEM image of CoCe–O–Ir_{SA} and the extracted line profiles from the regions highlighted with blue (x-y), green (m-n), and yellow (a-b) rectangles. The spots in the red dashed circles are ascribed to Ir SAs. **g** Formation energies (ΔE) of Ir SAs in lattice and adsorbed on the lattice. **h** The illustration of structure evolution. The H atoms of the substrates are omitted for clarity. Source Data are provided as a Source Data file.

phases are the actual active structures, which is in good agreement with the previously reported results[27,28]. The obtained sample after the electrochemical reconstruction is denoted as CoCe–O–Ir_{SA} for clarity based on the structural characterization results below.

Moreover, the Ir L_3-edge XANES spectrum of CoCe–O–Ir_{SA} is displayed in Fig. 3c. The FT-EXAFS spectrum and corresponding fitting results of CoCe–O–Ir_{SA} exhibit one prominent Ir–O bond at 1.99 Å in the first shell with a coordination number of about 6 (Fig. 3d and Supplementary Table 5). Compared with the corresponding results of CoCe–O–Ir, it is demonstrated that the reconstructed Ir species in CoCe–O–Ir_{SA} are well connected to the CoCeOOH support through IrO_6 coordination accompanied by the dechlorination (Supplementary Fig. 22)[29]. The disengagement of Cl after reconstruction is also affirmed by a comparison of the survey and Cl 2*p* XPS spectra between CoCe–O–Ir and CoCe–O–Ir_{SA} based on the apparent disappearance of the Cl element signal (Supplementary Fig. 23)[22].

To gain more insight into the structural evolution, AC-HAADF-STEM was conducted for CoCe–O–Ir_{SA} to observe the atomic-scale structural evolution. Surprisingly, it reveals uniformly atomic Ir dispersions on the support with high coverage (Fig. 3e). The mean density of Ir single atoms is about 52 per 10 nm^2 (Supplementary Fig. 24). Also, HRTEM and AC-HAADF-STEM images at a selected large area show no remaining clusters or generated particles on the reconstructed supports (Supplementary Fig. 25). To further confirm the homogeneity of Ir SAs existence, the AC-HAADF-STEM images from various areas were examined, revealing the well-dispersion of high-density Ir SAs in the sample (Supplementary Fig. 26). The HAADF-STEM image and corresponding mapping demonstrate the uniform elemental distribution (i.e., Co, Ce, O, Ir) without aggregations (Supplementary Fig. 27)[30]. Besides, no Ir–Ir signals at around 2.7 Å is discerned in the EXAFS fitting results, further demonstrating the well-dispersion of Ir SAs without metallic interaction in CoCe–O–Ir_{SA} (Supplementary Table 5)[31].

Meanwhile, the loading amount of Ir slightly changes from 2.61 wt.% to 2.38 wt.% determined by the inductively coupled plasma-mass spectroscopy (ICP-MS) analysis, implying the negligible dissolution of Ir element during the reconstruction process. The crystalline region of reconstructed support exhibits an interplanar spacing of 0.24 nm, which can be ascribed to the exposed (100) planes of CoCeOOH (Fig. 3f). Interestingly, the average distance between Ir SAs and adjacent metal atoms was measured to be about 0.29 nm, which is almost equal to the theoretical metal atomic distance (0.285 nm) of the CoCeOOH lattice (Supplementary Fig. 28). Meanwhile, this observation is also close to the EXAFS fitting result that the distance of Ir–M (M = Co, Ce, or Ir) bond is about 2.99 Å in the second shell (Supplementary Table 5).

As a rule of thumb, the reconstructed status of Ir SAs could be (i) anchored in the CoCeOOH lattice at a metal position connected with O atoms or (ii) adsorbed on the metal site of CoCeOOH atop in $Ir(OH)_6^{2-}$ form[29]. In this regard, we conducted density functional theory (DFT) calculations to estimate the formation energy (ΔE) for these two possible structures (Fig. 3g). A much lower ΔE (−0.928 eV) was obtained as the Ir SAs anchored in the CoCeOOH lattice. The higher ΔE for another structure may be caused by the electrostatic repulsion between the inner-layer metal atom and Ir atoms, resulting in lower stability[32]. Therefore, a more explicit mechanism of the evolution of the active OER structure is proposed in Fig. 3h. With the $CoCe(OH)_2$ nanosheets reconstructed into CoCeOOH nanosheets, the deposited metastable IrO_x clusters are disintegrated into Ir SAs accompanying the co-existed Ir SAs dechlorinated, both of which are incorporated into the lattice of CoCeOOH as high-density single-atom status with thermodynamic stability. Besides, the CoCe–O–Ir_{SA} exhibits decent structural stability with well-sustained high-density Ir SAs after the long-term stability test (Supplementary Fig. 29) and seawater electrolysis test (Supplementary Fig. 30).

To further reinforce the proposed reconstruction mechanism, the evolution of the Co–O–Ir counterpart as a comparison was conducted and analyzed. The TEM images exhibit a significant diameter decrease of the IrO_x clusters from 2.63 nm to 0.88 nm before and after reconstruction (Supplementary Figs. 31–33). This phenomenon underpins the generality of the strategy that the reconstruction of metastable hydroxides can induce the atomic-scale evolution of metastable IrO_x clusters during the OER. In turn, the existence of the Ce element leads to the symmetry-breaking of the Co substrate, owing to its intrinsic large-radius feature, which is critical to fragmenting metastable IrO_x into SAs thoroughly. Meanwhile, the morphological evolutions of the CoCe–O–Ir counterparts (i.e., CoCe–O–Ir–12 h and CoCe–O–Ir–48 h) were explored. It is found that the only existence of isolated Ir sites with the disengagement of Cl for the CoCe–O–Ir–12 h counterparts after the reconstruction process (Supplementary Fig. 34), which is consistent with the observations of the above optimal CoCe–O–Ir sample (i.e., CoCe–O–Ir–24 h). Besides, based on the ICP-MS measurements, the Ir loading amount changes from 1.75 wt.% to 1.59 wt.% for CoCe–O–Ir–12 h with negligible dissolution. For the CoCe–O–Ir–48 h after the reconstruction process, its loading amount of Ir also slightly changes from 3.36 wt.% to 3.24 wt.%, indicating the rich interaction sites of CoCe substrates. However, the tiny clusters still exist due to excessive metastable IrO_x clusters forming with the prolonged impregnation time (Supplementary Fig. 35). These results further confirm that the metastable Ir species on the symmetry-breaking $CoCe(OH)_2$ substrate simultaneously undergo reconstruction to form the SACs; with the suitable control of the metastable Ir species loadings, the high-density SACs can be obtained.

To illustrate the formation mechanism in-depth, we further deposited the metastable Ir intermediates on the stable and inert TiO_2 nanoparticles substrate through the identical impregnation method. The as-prepared IrO_x species are uniformly deposited on the surface of TiO_2 (Supplementary Fig. 36). After OER tests, the amount of Ir species is significantly decreased (Supplementary Table 6 and Supplementary Fig. 37). A portion of IrO_x clusters remains on the TiO_2 surface with a tendency of aggregation (Supplementary Fig. 38). Besides, the TiO_2 substrate exhibits well-defined unchanged lattice fringes and well-maintained Ti 2*p* XPS spectra (Supplementary Figs. 36–38). These results suggest that it is difficult to form effective and abundant metal-substrate interactions using stable TiO_2 support during reconstruction. In turn, it is demonstrated that two critical factors exist for the successful synthesis of high-density SACs: the formation of symmetry-breaking $CoCe(OH)_2$ substrates and simultaneously electrochemically induced reconstruction of metastable Ir intermediates.

In this regard, we extended our synthesis strategy to prepare other high-density SACs (CoLa–O–Ir_{SA} and NiCe–O–Ir_{SA}) using the substrates with different metal cations (La^{3+} and Ni^{2+}). Similar structural evolution processes were found through self-rearrangement of the CoLa–O–Ir and NiCe–O–Ir under identical OER processes (Supplementary Figs. 39–42). Specifically, the metastable Ir species on the symmetry-breaking $CoLa(OH)_2$ and $NiCe(OH)_2$ substrates (i.e., hetero-metastable phases) were self-reconstructed into the high-density Ir SAs confined into the ultrathin CoLaOOH and NiCeOOH nanosheets, demonstrating the generality of our strategy.

To explore the relationship between reaction kinetics and electron transfer, we first performed the operando electrochemical impedance spectroscopy (EIS) at different applied biases[33]. In Bode plots, the high-frequency (HF) region is related to the oxidation of the electrocatalyst, and the low-frequency (LF) one reflects the electron transfer from the electrolyte to the catalytic layer. As revealed in Fig. 4a, when the potential increases from 1.1 to 1.25 V vs. RHE on CoCe–O–Ir, the sharp disappearance of phase angle in the HF region demonstrates the fast reconstruction of the original $CoCe(OH)_2$ co-loaded IrO_x clusters and Ir SAs into the actual active structure as CoCe–O–Ir_{SA}. In Fig. 4b, as a comparison, the phase angle in the HF region for the CoCe sample was not changed, indicating that the co-loading of metastable Ir species can participate and facilitate the reconstruction of the CoCe substrates during the OER. Moreover, at the LF region with the potential >1.25 V vs. RHE (Fig. 4c), the peak frequency of CoCe–O–Ir_{SA} is higher than that of CoCe, suggesting a faster electron transfer rate from the intermediate species to the electrocatalyst after the introduction of embedded Ir SAs[34]. Meanwhile, the CoCe–O–Ir_{SA} achieves a lower phase angle than that of CoCe, demonstrating that incorporating Ir SAs can promote oxygen desorption[35].

The DFT calculations were further conducted to investigate the underlying catalytic reaction mechanism (Supplementary Data 1). The optimized CoOOH, CoCeOOH, and CoCe–O–Ir_{SA} configurations are displayed in Supplementary Fig. 43. The 3D and 2D profiles of differential charge density on CoCe–O–Ir_{SA} visualize a pronounced charge redistribution along the chemical bonds with more electrons delocalized around Ir atoms, suggesting that the incorporation of Ir SAs can regulate the electronic structure and thus achieve an enhanced catalytic ability (Fig. 4d, e)[36]. Moreover, the projected density of states (PDOS) indicates a strong orbital overlap between Co 3*d*, Ir 5*d*, O 2*p*, and Ce 4*f* orbitals (Fig. 4f)[37]. The CoCe–O–Ir_{SA} also exhibits higher occupation near the Fermi level (E_f) than CoCeOOH. The results demonstrate the strong *p*–*d*–*f* orbital couplings as the Ir SAs embedded in the CoCeOOH lattice. This leads to a promoted electron transport with a more conductive electronic structure for fast OER kinetics[38]. Furthermore, based on the *d*-band center theory, the more antibonding state is occupied below the Fermi level as the *d*-band center is downshifted. The average *d*-band center values for CoOOH, CoCeOOH, and CoCe–O–Ir_{SA} are −1.41, −1.46, and −1.52 eV, respectively (Fig. 4g). In this regard, Ir SAs endow the *d*-band center of CoCe–O–Ir_{SA} with more negativity, effectively weakening binding strength with reaction intermediates[39].

https://doi.org/10.1038/s41467-025-58163-0

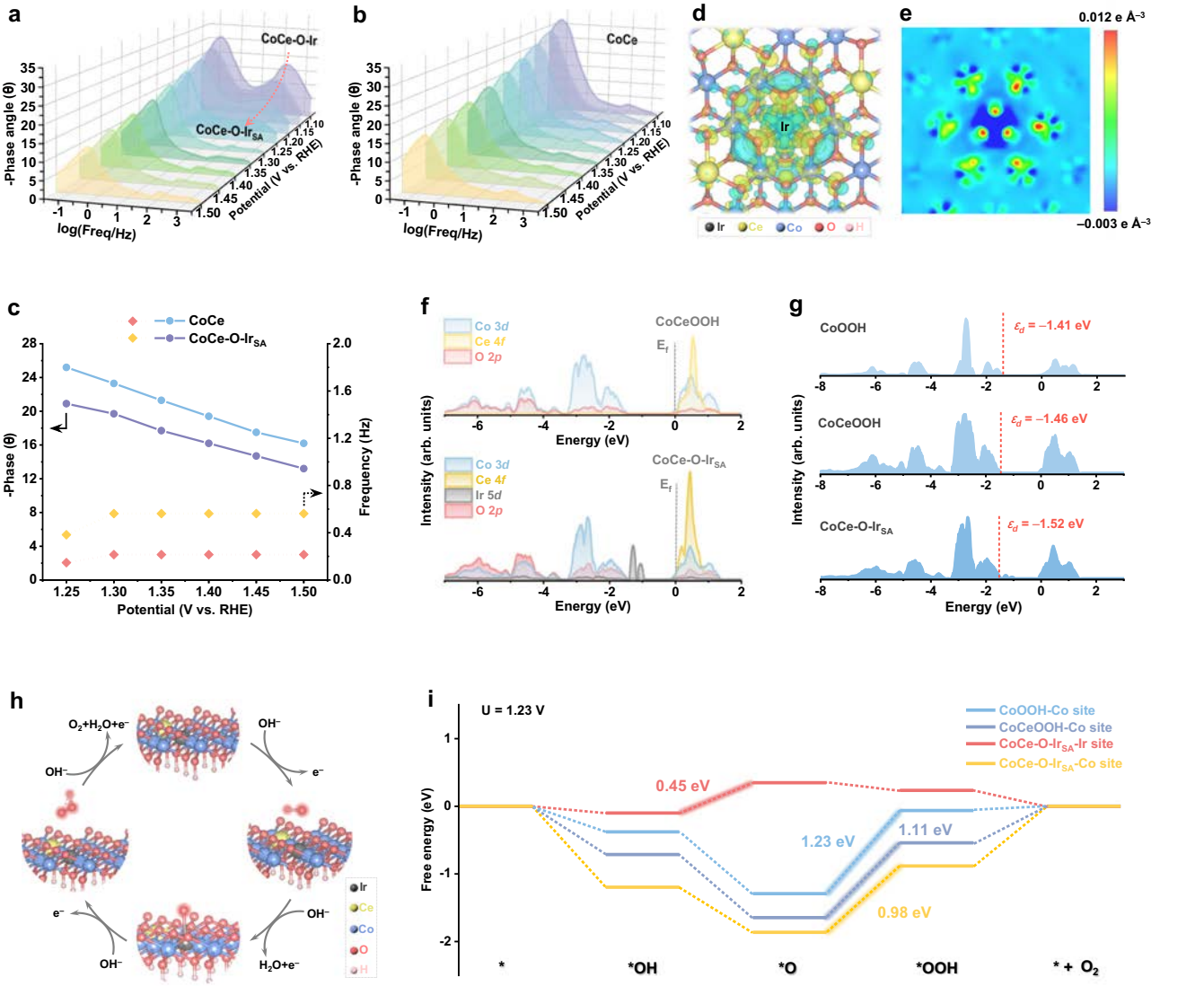

Fig. 4 | Exploration of the OER mechanism. Bode plots of CoCe–O–Ir (**a**) and CoCe (**b**) under different potentials. **c** Comparison of phase value and frequency of CoCe–O–Ir and CoCe at 1.25–1.50 V vs. RHE. 3D (**d**) and 2D profile (**e**) of differential charge density for CoCe–O–Ir$_{SA}$. The yellow and cyan regions in (**d**) represent electron accumulation and depletion, respectively. The red and blue regions in (**e**) represent electron accumulation and depletion, respectively. **f** PDOS of CoCeOOH and CoCe–O–Ir$_{SA}$. **g** *d*-band center of CoOOH, CoCeOOH, and CoCe–O–Ir$_{SA}$. **h** The schematic OER pathway for the Ir site of CoCe–O–Ir$_{SA}$. **i** Free-energy diagrams on different sites under an applied potential of 1.23 V. Source Data are provided as a Source Data file.

Free-energy diagrams of the OER at 1.23 V were calculated on the different sites following four concerted proton–electron transfer pathways (Fig. 4h). The limiting reaction barrier is decided by the free energy of the rate-determining step (RDS), which is an important evaluation for catalytic performance[40]. As depicted in Fig. 4i, for the Co site in CoOOH, the RDS is the formation of *OOH with a limiting barrier as large as 1.23 eV. Meanwhile, the Co site in CoCeOOH displays the same RDS with a lower limiting barrier of 1.11 eV, suggesting the dual metal oxyhydroxides are more beneficial for upgrading with OER activity than pure oxyhydroxides. Furthermore, for the Co site in CoCe–O–Ir$_{SA}$, the RDS of *OOH formation exhibits a limiting barrier of 0.98 eV. Meanwhile, the limiting barrier of the Ce site in CoCe–O–Ir$_{SA}$ (1.01 eV) is also reduced as compared to that in CoCeOOH (1.19 eV) (Supplementary Fig. 44). The single Ir site in CoCe–O–Ir$_{SA}$ shows the lowest limiting barrier of 0.45 eV as the RDS is the conversion of *OH to *O. Therefore, for the CoCe–O–Ir$_{SA}$, the Ir SAs act as the main active site for driving OER; meanwhile, the Co and Ce sites are also activated with lower energy barriers for the RDS after the introduction of Ir as compared to those in the pure CoCeOOH owing to the optimized electronic structures, synergistically contributing to a more favorable OER activity[41].

In summary, we have synthesized the high-density Ir SAs anchored in the ultrathin CoCeOOH nanosheets as a thermodynamic-stable high-active structure, which is self-rearranged from the metastable Ir-based intermediates supported by symmetry-broken CoCe(OH)$_2$. The resulting CoCe–O–Ir$_{SA}$ exhibits a high OER activity in 1.0 M KOH, delivering an overpotential of 187 mV at 100 mA cm^{-2} and steady operation for 1000 h at 500 mA cm^{-2}, which is superior to almost all state-of-the-art reported electrocatalysts. Moreover, when applied as an anode in an AEMWE system, the CoCe–O–Ir$_{SA}$ can demonstrate steady seawater splitting at 500 mA cm^{-2} for 150 h. The operando experiments and theoretical calculation reveal that the reconstructed Ir SAs are highly active sites for OER, which can facilitate electron transfer by strongly *p–d–f* orbital couplings, reduce the free energy of the rate-determining step, and improve the intrinsic activity of Co/Ce atoms, thus achieving notable OER performance. This work

will provide a guideline for quickly realizing stable single atoms with high density and superior performance for future industrial applications.

Methods

Chemicals and materials

Cobalt nitrate hexahydrate ($Co(NO_3)_2{\cdot}6H_2O$, 99%), cerium nitrate hexahydrate ($Ce(NO_3)_3{\cdot}6H_2O$, 99.99%), nickel nitrate hexahydrate ($Ni(NO_3)_2{\cdot}6H_2O$, 99%), and potassium hydroxide (KOH, 99%) were purchased from Meryer Chemical Technology Co., Ltd. Lanthanum nitrate hexahydrate ($La(NO_3)_3{\cdot}6H_2O$, 99%) was purchased from Shanghai Aladdin Biochemical Technology Co., Ltd. Iridium chloride hydrate ($IrCl_3{\cdot}xH_2O$, 99.99%) and 2-methylimidazole ($C_4H_6N_2$, 99%) were purchased from Acros Organics CO. Acetonitrile (CH_3CN, ≥99.9%) was purchased from RCI Labscan Ltd. Nickel foam (NF, thickness: 1 mm) and anion-exchange membrane (AEM, Dioxide Materials Sustainion X37-50 gradeT, thickness: 50 μm) were purchased from Fuel Cell Store Co. Deionized water (DI water) was obtained locally for the experiments. The natural seawater was obtained from Cheung Chau in Hong Kong and filtered to remove visible impurities before its utilization.

Sample synthesis

Synthesis of CoCe double hydroxides (denoted as CoCe). 1.9 mmol $Co(NO_3)_2{\cdot}6H_2O$ and 0.1 mmol $Ce(NO_3)_3{\cdot}6H_2O$, and 4 mmol 2-methylimidazole were added into 80 mL solution containing acetonitrile and water (3:1 v/v). Meanwhile, the NF (2×2 cm^2) is fixed and vertically immersed in the solution. The solution was stirred for 1 h at room temperature, and then the CoCe-coated NF substrate was taken out, rinsed with water and ethanol, and dried overnight at 60 °C in an oven. The mass loading of CoCe was determined to be about 1.0 mg cm^{-2} according to the weight increase on the NF.

Synthesis of metastable iridium species decorated CoCe (denoted as CoCe–O–Ir). The as-prepared CoCe nanosheet arrays grown on NF (0.5×2 cm^2) electrode was immersed into 2 mL aqueous solution containing $IrCl_3{\cdot}xH_2O$ (1 mg mL^{-1}) for 24 h and then taken out and dried at 60 °C in an oven overnight.

Synthesis of Co hydroxides (denoted as Co). The synthesis procedure of Co nanosheet arrays supported on NF was the same as that of CoCe nanosheet arrays, except for adding 2 mmol $Co(NO_3)_2{\cdot}6H_2O$ without adding $Ce(NO_3)_3{\cdot}6H_2O$.

Synthesis of metastable iridium species decorated Co (denoted as Co–O–Ir). The synthesis procedure of Co–O–Ir was the same as that of CoCe–O–Ir, except for using Co nanosheet arrays as a precursor to replacing CoCe nanosheet arrays.

Synthesis of CoLa double hydroxides (denoted as CoLa). The synthesis procedure of CoLa nanosheet arrays supported on NF was the same as that of CoCe nanosheet arrays, except for adding 1.9 mmol $Co(NO_3)_2{\cdot}6H_2O$ and 0.1 mmol $La(NO_3)_3{\cdot}6H_2O$.

Synthesis of metastable iridium species decorated CoLa (denoted as CoLa–O–Ir). The synthesis procedure of CoLa–O–Ir was the same as that of CoCe–O–Ir, except for using CoLa nanosheet arrays as a precursor to replacing CoCe nanosheet arrays.

Synthesis of NiCe double hydroxides (denoted as NiCe). The synthesis procedure of NiCe nanosheet arrays supported on NF was the same as that of CoCe nanosheet arrays, except for adding 1.9 mmol $Ni(NO_3)_2{\cdot}6H_2O$ and 0.1 mmol $Ce(NO_3)_3{\cdot}6H_2O$.

Synthesis of metastable iridium species decorated NiCe (denoted as NiCe–O–Ir). The synthesis procedure of NiCe–O–Ir was the same as that of CoCe–O–Ir, except for using NiCe nanosheet arrays as a precursor to replacing CoCe nanosheet arrays.

Characterizations

FEI Quanta 450 equipment was applied to collect the SEM images. TEM, HRTEM, HAADF-STEM, and corresponding elemental mapping results were performed on a JEM-2100F instrument with an accelerating voltage of 200 kV. AC-HAADF-STEM was carried out on the Thermo Themis Z instrument at an accelerating voltage of 300 kV. A Nanoscope IIIA system was used to measure the AFM spectra. The Si platelets were used as substrates for the dispersion of nanosheets for the AFM tests. A Bruker D8 Advance powder diffractometer was applied to record XRD patterns. A PE optima 6000 spectrometer was utilized to measure ICP-MS. XPS was conducted using Thermo Fisher ESCALAB 250Xi equipment. C 1*s* peak at 284.8 eV was used to calibrate all binging energies. The Ir L_3-edge X-ray absorption fine structure (XAFS) measurements for the CoCe–O–Ir sample were conducted with Si (111) crystal monochromators at the 5S1 X-ray absorption beamline at the Aichi Synchrotron Radiation Center (AichiSR) (Japan). The data was collected in fluorescence mode. The XAFS spectra of the standard samples (i.e., Ir foil and IrO_2) were collected in transmission mode. The Ir L_3-edge XAFS measurements for the CoCe–O–Ir_{SA} sample were carried out with Si (111) crystal monochromators at the BL14W Beamline at the Shanghai Synchrotron Radiation Facility (SSRF) (Shanghai, China). A 32-element Ge detector was applied to record XAFS spectra at room temperature. The data was recorded in fluorescence mode. The XAFS spectra of the standard samples were recorded in fluorescence mode. Data reduction, data analysis, and EXAFS fitting were processed by the Athena and Artemis programs in the Demeter data analysis packages[42] that utilized the FEFF6 program[43].

Electrochemical tests

All electrochemical measurements were conducted on an electrochemical workstation (CHI 660E) with a high-current amplifier (CHI 680C). The electrolyte was 1.0 M KOH (pH = 13.69 ± 0.02). For the preparation of 1.0 M KOH, 56.11 g KOH solid was dissolved in 500 mL DI water with stirring for 20 min; then, the solution was transferred into 1 L volumetric flask by adding DI water to the volume. Finally, the 1.0 M KOH solution was stored in polyethylene bottles at room temperature. For a standard three-electrode setup, the catalyst/NF sample was directly applied as a working electrode with a geometric area of 0.5 cm^2 (i.e., 0.5×1 cm) immersed into the electrolyte. A graphite rod was employed as the counter electrode. A Hg/HgO electrode or an Ag/AgCl electrode with a salt bridge was used as the reference electrode. For the benchmark samples, 5 mg of IrO_2 was dispersed into a solution containing 450 μL of ethanol and 50 μL of Nafion solution (5 wt%), followed by 2 h of sonication to produce a homogeneous ink. Subsequently, 50 μL of ink was drop-casted onto a pure NF surface (geometric area: 0.5×1 cm; mass loading: 1 mg cm^{-2}).

Before the electrochemical measurement, the Ar flow was purged into the electrolyte for 30 min. Cyclic voltammetry (CV) curves consisting of forward and backward scans were tested at a scan rate of 5 mV s^{-1}. The backward scans of the CV curves were used as polarization curves to evaluate the OER performance. The polarization curves were presented with *iR* corrections. *iR* corrections were conducted based on the formula: $E_{iR} = E_0 - iR$, where the solution resistance (i.e., R) is 0.64 ± 0.19 Ω determined by EIS. EIS tests were performed from 100,000 to 0.01 Hz at an amplitude of 5 mV. CV curves were recorded at various scan rates (i.e., 20, 40, 60, 80, 100 mV s^{-1}) within the potential range of 0.8 to 0.9 V vs. RHE to assess the C_{dl} values. The CP tests at 500 mA cm^{-2} without *iR* compensation were applied to determine the long-term stability of catalysts.

The AEMWE test was measured in 1.0 M KOH and seawater as an electrolyte (pH = 13.70 ± 0.03) at room temperature with a 10 mL min^{-1} flow rate. The catalyst/NF sample was applied as an anode with a geometric area of 1 cm^2 (i.e., 1 × 1 cm). The commercial NiFeCo/Ni fiber was used as a cathode with the same geometric area. The CP tests at 500 mA cm^{-2} without *iR* compensation were applied to measure the long-term stability of catalysts in alkaline seawater.

RHE calibration

The calibration of a reference electrode concerning a reversible hydrogen electrode (RHE) was conducted using a three-electrode system with a working electrode (Pt foil), counter electrode (Pt foil), and reference electrode (Hg/HgO or Ag/AgCl electrode) in the H_2-saturated electrolyte (1.0 M KOH). The thermodynamic potential for the hydrogen electrode reactions was determined to be the average of the two potentials at which the current crossed zero (Supplementary Fig. 9)[44]. Therefore, in 1.0 M KOH, the obtained calibration equations are $E_{RHE} = E_{Hg/HgO} + 0.9065$ V and $E_{RHE} = E_{Ag/AgCl} + 1.002$ V.

Faradaic efficiency measurement

A typical drainage method was applied to detect the generated oxygen gas amount for alkaline seawater splitting (Supplementary Fig. 21). The chronopotentiometry was conducted at 500 mA cm^{-2} to maintain constant gas generation. The volume of extruded water by generated gas was recorded every 5 min. The process was performed once under controlled experimental conditions.

In-situ Raman spectroscopy

A WITec alpha 300R Raman system was applied to conduct the in-situ Raman measurements at a laser wavelength of 532 nm. The in-situ electrochemical cell was made from Teflon and equipped with a quartz window (Supplementary Fig. 45). The electrolyte (i.e., 1.0 M KOH) was filled in the electrochemical cell. The catalyst grown on NF was shaped into a plate as the working electrode (diameter: ~6 mm; geometric area: ~0.28 cm^2). The counter and reference electrodes were platinum wire and an Ag/AgCl electrode, respectively. The three electrodes were connected to an electrochemical workstation (CHI 760E). Raman spectra were recorded at different potentials from 1.00 V to 1.50 V vs. RHE in increments of 0.05 V. Each applied potential lasts 5 min.

Theoretical computation details

The first-principle calculations based on DFT were conducted using the Vienna Ab initio Simulation Package (VASP)[45], incorporating the full-potential projected augmented wave (PAW) method[46]. The exchange-correlation interactions were treated within the generalized gradient approximation using the Perdew-Burke-Ernzerhof functional (GGA-PBE)[47]. The DFT + U method was applied to treat localized Co 3*d* and Ce 4*f* orbitals with U = 3.3[48] and 4.0[49], respectively. A vacuum layer of 20 Å was introduced to eliminate interactions between periodic surfaces. The cutoff energy was established as 450 eV for the plane-wave expansion. The self-consistent field (SCF) calculations were performed with an energy convergence threshold of 10^{-5} eV. At the same time, atomic structures were optimized until the maximum force on each atom was below 0.01 eV/Å. Density of State (DOS) calculations utilized a Γ-centered *k*-point mesh of 5 × 5 × 1.

The OER mechanism was described by the four-electron transfer pathways as follows:

$$OH^- + * \rightarrow *OH + e^-$$

$$*OH + OH^- \rightarrow *O + H_2O + e^-$$

$$*O + OH^- \rightarrow *OOH + e^-$$

$$*OOH + OH^- \rightarrow * + O_2 + H_2O + e^-$$

where the symbol '*' represents the active site on the surface, *OH, *O, *OOH are the adsorbed intermediates.

The free-energy changes of the OER process can be calculated as follows:

$$\Delta G = \Delta E + \Delta ZPE - T\Delta S$$

where ΔE is the DFT-calculated binding energy change of the intermediates; ΔZPE is the difference in zero-point energy; ΔS is the change in entropy at T = 298 K obtained from vibrational frequency calculations. The free energy of gaseous O_2 is derived as $G(O_2) = 2\,G(H_2O) - 2\,G(H_2) + 4.92$ (eV). The free energy at an applied potential U is calculated using the equation $G_U = G - neU$, where n represents the number of transferred proton-electron pairs and e represents the elemental charge of an electron.

Data availability

Relevant data generated in this study are provided in the Article/Supplementary Information/Source Data file. Source data are provided with this paper.

References

1. Nong, H. N. et al. Key role of chemistry versus bias in electrocatalytic oxygen evolution. *Nature* **587**, 408–413 (2020).
2. Li, X. et al. Microenvironment modulation of single-atom catalysts and their roles in electrochemical energy conversion. *Sci. Adv.* **6**, eabb6833 (2020).
3. Wang, Q. et al. Coordination engineering of iridium nanocluster bifunctional electrocatalyst for highly efficient and pH-universal overall water splitting. *Nat. Commun.* **11**, 4246 (2020).
4. Zhou, Y. et al. Multilayer stabilization for fabricating high-loading single-atom catalysts. *Nat. Commun.* **11**, 5892 (2020).
5. Datye, A. K. & Guo, H. Single atom catalysis poised to transition from an academic curiosity to an industrially relevant technology. *Nat. Commun.* **12**, 895 (2021).
6. Moliner, M. et al. Reversible transformation of Pt nanoparticles into single atoms inside high-silica chabazite zeolite. *J. Am. Chem. Soc.* **138**, 15743–15750 (2016).
7. Zhang, N. et al. Silver single-atom catalyst for efficient electrochemical CO_2 reduction synthesized from thermal transformation and surface reconstruction. *Angew. Chem. Int. Ed.* **60**, 6170–6176 (2021).
8. Liu, K. et al. Strong metal-support interaction promoted scalable production of thermally stable single-atom catalysts. *Nat. Commun.* **11**, 1263 (2020).
9. Liu, X. et al. Comprehensive understandings into complete reconstruction of precatalysts: synthesis, applications, and characterizations. *Adv. Mater.* **33**, 2007344 (2021).
10. Wang, Q. et al. Single iridium atom doped Ni_2P catalyst for optimal oxygen evolution. *J. Am. Chem. Soc.* **143**, 13605–13615 (2021).
11. Jang, H. & Lee, J. Iridium oxide fabrication and application: a review. *J. Energy Chem.* **46**, 152–172 (2020).
12. Quan, Q. et al. Topochemical domain engineering to construct 2D mosaic heterostructure with internal electric field for high-performance overall water splitting. *Nano Energy* **101**, 107566 (2022).
13. Wang, Y. et al. Nano-metal diborides-supported anode catalyst with strongly coupled TaO_x/IrO_2 catalytic layer for low-iridium-loading

proton exchange membrane electrolyzer. *Nat. Commun.* **14**, 5119 (2023).
14. Liu, Z., Ma, R., Osada, M., Takada, K. & Sasaki, T. Selective and controlled synthesis of α- and β-cobalt hydroxides in highly developed hexagonal platelets. *J. Am. Chem. Soc.* **127**, 13869–13874 (2005).
15. Wang, J., Wei, Z., Mao, S., Li, H. & Wang, Y. Highly uniform Ru nanoparticles over N-doped carbon: pH and temperature-universal hydrogen release from water reduction. *Energy Environ. Sci.* **11**, 800–806 (2018).
16. Zhang, J. Y. et al. Local spin-state tuning of cobalt-iron selenide nanoframes for the boosted oxygen evolution. *Energy Environ. Sci.* **14**, 365–373 (2021).
17. Xu, H. et al. Fabrication of layered double hydroxide microcapsules mediated by cerium doping in metal–organic frameworks for boosting water splitting. *Energy Environ. Sci.* **13**, 2949–2956 (2020).
18. Chen, R.-S., Korotcov, A., Huang, Y.-S. & Tsai, D.-S. One-dimensional conductive IrO_2 nanocrystals. *Nanotechnology* **17**, R67 (2006).
19. Wang, C. et al. Engineering lattice oxygen activation of iridium clusters stabilized on amorphous bimetal borides array for oxygen evolution reaction. *Angew. Chem. Int. Ed.* **60**, 27126–27134 (2021).
20. Zhou, K. L. et al. Platinum single-atom catalyst coupled with transition metal/metal oxide heterostructure for accelerating alkaline hydrogen evolution reaction. *Nat. Commun.* **12**, 3783 (2021).
21. Zhang, Z. et al. Selectively anchoring single atoms on specific sites of supports for improved oxygen evolution. *Nat. Commun.* **13**, 2473 (2022).
22. He, Q. et al. Confining high-valence iridium single sites onto nickel oxyhydroxide for robust oxygen evolution. *Nano Lett.* **22**, 3832–3839 (2022).
23. Guan, J. et al. Synthesis and demonstration of subnanometric iridium oxide as highly efficient and robust water oxidation catalyst. *ACS Catal.* **7**, 5983–5986 (2017).
24. Wang, J. et al. Dynamically adaptive bubbling for upgrading oxygen evolution reaction using lamellar fern-like alloy aerogel self-standing electrodes. *Adv. Mater.* **36**, e2307925 (2024).
25. Fan, L. et al. High entropy alloy electrocatalytic electrode toward alkaline glycerol valorization coupling with acidic hydrogen production. *J. Am. Chem. Soc.* **144**, 7224–7235 (2022).
26. Wang, F. et al. Activating lattice oxygen in high-entropy LDH for robust and durable water oxidation. *Nat. Commun.* **14**, 6019 (2023).
27. Quan, Q. et al. Self-anti-stacking 2D metal phosphide loop-sheet heterostructures by edge-topological regulation for highly efficient water oxidation. *Small* **17**, 2006860 (2021).
28. Yin, Z. H. et al. Ir single atoms boost metal-oxygen covalency on selenide-derived NiOOH for direct intramolecular oxygen coupling. *J. Am. Chem. Soc.* **146**, 6846–6855 (2024).
29. Wei, J. et al. Site-specific metal-support interaction to switch the activity of Ir single atoms for oxygen evolution reaction. *Nat. Commun.* **15**, 559 (2024).
30. Hai, X. et al. Scalable two-step annealing method for preparing ultra-high-density single-atom catalyst libraries. *Nat. Nanotechnol.* **17**, 174–181 (2022).
31. Zhao, J. et al. A heterogeneous iridium single-atom-site catalyst for highly regioselective carbenoid O–H bond insertion. *Nat. Catal.* **4**, 523–531 (2021).
32. Feng, C. et al. Tuning the electronic and steric interaction at the atomic interface for enhanced oxygen evolution. *J. Am. Chem. Soc.* **144**, 9271–9279 (2022).
33. Liu, C. et al. S-species-evoked high-valence $Ni^{2+\delta}$ of the Evolved beta-$Ni(OH)_2$ electrode for selective oxidation of 5-hydroxymethylfurfural. *Adv. Mater.* **35**, e2211177 (2023).
34. Zou, X. et al. Screening spinel oxide supports for RuO_2 to boost bifunctional electrocatalysts for advanced Zn–air batteries. *Adv. Funct. Mater.* **34**, 2401134 (2024).
35. Zheng, Q., Yan, Y., Zhong, J., Yan, S. & Zou, Z. Reagent-Adaptive Active Site Switching on the $IrO_x/Ni(OH)_2$ Catalyst. *Energy Environ. Sci.* **17**, 748–759 (2024).
36. Quan, Q. et al. Multiscale confinement engineering for boosting overall water splitting by one-step stringing of a single atom and a Janus nanoparticle within a carbon nanotube. *ACS Nano* **18**, 1204–1213 (2024).
37. Zeng, Z. et al. Orbital coupling of hetero-diatomic nickel-iron site for bifunctional electrocatalysis of CO_2 reduction and oxygen evolution. *Nat. Commun.* **12**, 4088 (2021).
38. Li, G. et al. The synergistic effect of Hf-O-Ru bonds and oxygen vacancies in Ru/HfO_2 for enhanced hydrogen evolution. *Nat. Commun.* **13**, 1270 (2022).
39. Zhu, Y. et al. Facilitating alkaline hydrogen evolution reaction on the hetero-interfaced Ru/RuO_2 through Pt single atoms doping. *Nat. Commun.* **15**, 1447 (2024).
40. Fei, H. et al. General synthesis and definitive structural identification of MN_4C_4 single-atom catalysts with tunable electrocatalytic activities. *Nat. Catal.* **1**, 63–72 (2018).
41. Zhu, Y. et al. Iridium single atoms incorporated in Co_3O_4 efficiently catalyze the oxygen evolution in acidic conditions. *Nat. Commun.* **13**, 7754 (2022).
42. Ravel, B. & Newville, M. ATHENA, ARTEMIS, HEPHAESTUS: data analysis for X-ray absorption spectroscopy using IFEFFIT. *J. Synchrotron. Radiat.* **12**, 537–541 (2005).
43. Zabinsky, S. I., Rehr, J. J., Ankudinov, A., Albers, R. C. & Eller, M. J. Multiple-scattering calculations of X-ray-absorption spectra. *Phys. Rev. B* **52**, 2995–3009 (1995).
44. Liang, Y. et al. Co_3O_4 nanocrystals on graphene as a synergistic catalyst for oxygen reduction reaction. *Nat. Mater.* **10**, 780–786 (2011).
45. Kresse, G. & Furthmüller, J. Efficient iterative schemes for ab initio total-energy calculations using a plane-wave basis set. *Phys. Rev. B* **54**, 11169–11186 (1996).
46. Blöchl, P. E. Projector augmented-wave method. *Phys. Rev. B* **50**, 17953–17979 (1994).
47. Perdew, J. P., Burke, K. & Ernzerhof, M. Generalized gradient approximation made simple. *Phys. Rev. Lett.* **77**, 3865–3868 (1996).
48. Zhou, J. et al. Electrochemically accessing ultrathin Co (oxy)-hydroxide nanosheets and operando identifying their active phase for the oxygen evolution reaction. *Energy Environ. Sci.* **12**, 739–746 (2019).
49. Huang, B., Gillen, R. & Robertson, J. Study of CeO_2 and its native defects by density functional theory with repulsive potential. *J. Phys. Chem. C* **118**, 24248–24256 (2014).

Acknowledgements

This work was financially supported by the City University of Hong Kong (project no. 7020088, 9229138, 9231502, and 9231539). Open Access made possible with partial support from the Open Access Publishing Fund of the City University of Hong Kong.

Author contributions

Q.Q. and J.C.H. conceived the idea and led the project. Q.Q., Y.Z., H.L., W.W. (Wei Wang), P.X., D.C., and C.Y. processed the sample growth and structural characterizations. Q.Q., W.W. (Weijun Wang), Y.M., D.Y., Y.L., and D.S. processed the electrochemical measurements. Y.Z., Q.Q., L.C., T.Y., and C.W. conducted DFT calculations. S.L., S.P.Y., and J.C.H. supervised the work. Q.Q. wrote the manuscript. All authors made revisions and approved the manuscript.

Competing interests

The authors declare no competing interests.

Additional information

Supplementary information The online version contains supplementary material available at https://doi.org/10.1038/s41467-025-58163-0.

Correspondence and requests for materials should be addressed to Shaohai Li, SenPo Yip or Johnny C. Ho.

Peer review information *Nature Communications* thanks Shiming Zhou and the other anonymous reviewer(s) for their contribution to the peer review of this work. A peer review file is available.

[1]Department of Materials Science and Engineering, City University of Hong Kong, Hong Kong SAR, China. [2]Department of Chemistry, City University of Hong Kong, Hong Kong SAR, China. [3]State Key Laboratory of Terahertz and Millimeter Waves, City University of Hong Kong, Hong Kong SAR, China. [4]Interdisciplinary Graduate School of Engineering Sciences, Kyushu University, Fukuoka, Japan. [5]China International Marine Containers Offshore Co., Ltd, Shenzhen, China. [6]Institute of Materials Research, Tsinghua Shenzhen International Graduate School, Tsinghua University, Shenzhen, China. [7]Institute for Materials Chemistry and Engineering, Kyushu University, Fukuoka, Japan. [8]Department of Applied Chemistry, Graduate School of Engineering, The University of Tokyo, Tokyo, Japan. [9]Present address: Department of Materials Science and Engineering, National University of Singapore, Singapore, Singapore. [10]These authors contributed equally: Quan Quan, Yuxuan Zhang. ✉e-mail: sh09.li@nus.edu.sg; yip.sen.po.472@m.kyushu-u.ac.jp; johnnyho@cityu.edu.hk